Available online at www.sciencedirect.com
SCIENCE DIRECT®
Journal of Nuclear Materials 335 (2004) 335–344
journal of nuclear materials
www.elsevier.com/locate/jnucmat

Impact properties of 304L stainless steel GTAW joints evaluated by high strain rate of compression tests

Woei-Shyan Lee [a,*], Chi-Feng Lin [b], Chen-Yang Liu [a], Fan-Tzung Tzeng [a]

[a] Department of Mechanical Engineering, National Cheng Kung University, Tainan 70101, Taiwan, ROC
[b] National Center for High-Performance Computing, Hsin-Shi, Tainan County 744, Taiwan, ROC

Received 25 November 2003; accepted 3 July 2004

Abstract

This paper presents an investigation into the high velocity impact of 304L stainless steel gas tungsten arc welded (GTAW) joints at strain rates between 10^{-3} and 7.5×10^3 s^{-1} using a compressive split-Hopkinson bar. The results show that the impact properties and fracture characteristics of the tested weldments depend strongly on applied strain rate. This rate-dependent behavior is in good agreement with model predictions using the hybrid Zerilli–Armstrong constitutive law. It is determined that the tested weldments fail as a result of adiabatic shearing. The fracture surfaces of the fusion zone and base metal regions are characterized by the presence of elongated dimples. The variation in the observed dimple features with strain rate is consistent with the results of the impact stress–strain curves.

PACS: 81.20.Vj; 81.70.Bt; 62.20.Fe

1. Introduction

Due to its anti-corrosion properties, and its ability to provide high strength within various product forms, 304L austenitic stainless steel is widely used for a diverse range of applications within a variety of different fields, including the chemical and automotive industries and the nuclear power plants. In the application of nuclear energy systems, the components made of 304L stainless steel are subjected to high strain rate loading, as a result of the sudden impact of foreign objects or any thermal shock incidence. This high strain rate loading may lead to a drastic change in deformation modes and failure mechanisms. Furthermore, these applications frequently require the welding of their constituent components, and consequently, the favorable welding characteristics of 304L SS play an important role in its selection as the material of choice. Previous researchers have demonstrated that 304L SS can be successfully welded using a variety of techniques, including gas tungsten arc welding, manual metal arc welding, submerged arc welding, and plasma arc welding [1–4]. In their operating environments, these welded components are often required to withstand a high rate of deformation as mentioned above. However, the microstructure and stress state characteristics of the welded joints differ from those of the base material, and the performance of the welded structure is usually limited by the initiation of failure within the heat affected zone (HAZ) of the base material, particularly within the coarse-grained region of the HAZ adjacent to the weld metal. Therefore, to ensure

* Corresponding author. Tel.: +886 6 2367008/2757575x 62101; fax: +886 6 2352973.
E-mail address: wslee@mail.ncku.edu.tw (W.-S. Lee).

0022-3115/$ - see front matter © 2004 Elsevier B.V. All rights reserved.
doi:10.1016/j.jnucmat.2004.07.031

the reliability of large-scale structures which will be subjected to dynamic impact loading conditions, it is essential to evaluate the mechanical properties of their structural materials, including their weld metals, under realistic operating conditions.

Previous investigations have made use of the split-Hopkinson bar or a variety of alternative shock loading apparatus to perform extensive studies into the mechanical behavior of various structural materials under high strain rate impact loading conditions [5–7]. In general, these studies have revealed that the strain rate has some degree of influence on the impact properties of most materials. Additionally, these studies have shown that an increasing strain rate causes a significant increase in the flow stress when the loading rate is high. Furthermore, there is considerable evidence to suggest that this strain rate dependence effect becomes even more marked at strain rates greater than approximately 10^3 s^{-1}. The increased strain rate sensitivity noted at high strain rates has been interpreted by different deformation mechanisms such as thermally activated mechanisms, viscous drag mechanisms, or the enhanced rate of dislocation generation [8,9]. Under high strain rate loading conditions, the plastic deformation process can be regarded as adiabatic. Consequently, deformation of the material is accompanied by a significant temperature rise, and the plastic strain is restricted to a narrow region of the material, generally referred to as the 'adiabatic shear band'. It is observed that the material within this shear band has a lower flow stress than the surrounding material. Furthermore, shear zones and internal cracks occur within the shear band, and become the sites of eventual failure when the material is subsequently subjected to dynamic impact loading. Several researchers have investigated the initiation of failure within the shear bands of a variety of different materials [10,11]. Meanwhile, the formation mechanisms of adiabatic shear, and the criterion for the instability of plastic flow have also been examined [12,13].

Although the dynamic impact properties and associated microstructures of austenitic stainless steel have been well documented [7,14–16], little work has been reported with regard to the impact behavior and fracture characteristics of austenitic stainless steel welded joints. Consequently, it is the intention of the present study to examine the impact behavior of 304L SS GTAW joints when subjected to compressive strain rates in the range of 10^{-3}–7.5×10^3 s^{-1}. The corresponding fracture evolutions in the fusion zone and base material regions are also investigated, and are correlated with the observed impact characteristics.

2. Experimental procedure

The base material adopted in the present study was 304L stainless steel purchased from Eastern Steel Corp. (Spring House, PA) in plate form. To remove the residual stress and obtain a uniform microstructure, the as-received base material plates were annealed at 1050 °C for 1 h and then allowed to cool in air. Welding was performed using a TGS-308L filler metal, which was supplied in the form of a spooled wire of 3.2 mm diameter, conforming to standard AWS A5.9-93 ER 308L. The chemical compositions of the base material and filler metal are provided in Table 1. The test weldments were prepared by using the manual gas tungsten arc welding (GTAW) process to butt-weld two annealed 304L SS plates with dimensions of $150^{l} \times 75^{w} \times 12^{t}$ mm. High purity argon gas was used during the welding process for shielding and backing purposes in order to enhance the quality of the weld. The adopted welding parameter details are presented in Table 2. Fig. 1 presents a schematic diagram of the welding configuration, in which it can be seen that two plates are welded together with a 3.2 mm root opening gap and a 1 mm root face to form a V-shaped joint groove with a 75° inclined angle. The joint was formed using a total of 14 separate

Table 1
Chemical compositions of base metal and filler metal (wt%)

Type	Wt%								
	C	Mn	Si	P	S	Cu	Ni	Cr	Mo
SUS304L	0.02	1.74	0.47	0.027	0.005	–	8.09	18.28	–
Filler metal (TGS-308L)	0.014	1.59	0.43	0.023	0.014	0.12	10.74	19.78	0.07

Table 2
Welding parameters for gas tungsten arc welding process

Current (A)	Voltage (V)	Welding speed ($mm\,min^{-1}$)	Electrod	Shield gas	Gas flow rate	Heat input ($kJ\,mm^{-1}$)	No. of passes
200	19	220	W–0.2Th	Argon	14 l/min	1.4	14

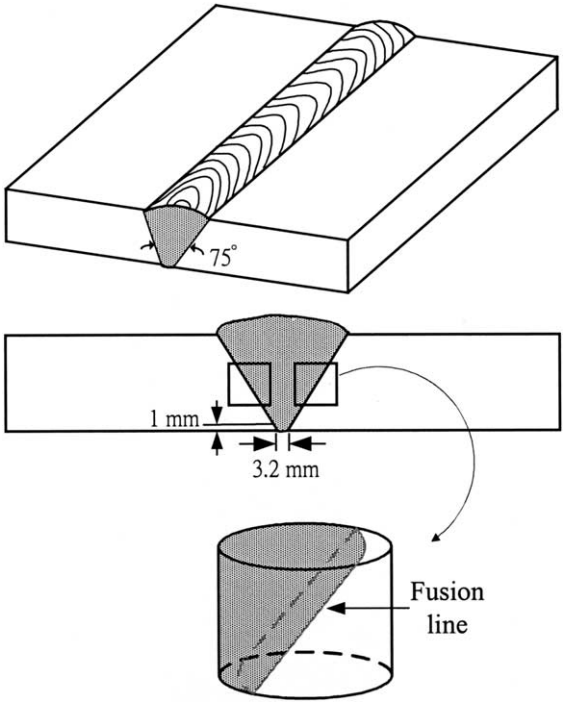

Fig. 1. Schematic representation of specimens used in TGAW welding.

welding passes. After completion of the welding process, cylindrical specimens measuring 10 mm in diameter by 10 mm in length were removed from the welded joint. As shown in Fig. 1, the location from which these specimens were taken was chosen such that each specimen would include material from the weld itself, the HAZ, and the original base metal. The end faces of the specimens were then lubricated with molybdenum disulphide grease to minimize friction effects during compression testing.

Quasi-static compression tests were conducted using a dynamic material testing system (MTS) at a strain rate of 10^{-3} s^{-1}. Subsequently, dynamic compression tests with high strain rates ranging from 1.5×10^{3} to 7.5×10^{3} s^{-1} were performed using a compressive split-Hopkinson bar apparatus [17] comprising an incident bar, a transmission bar made from 12 mm diameter maraging steel, and a striker bar. During compression testing, the specimens were located between the incident bar and the transmission bar, and the incident bar was then impacted by the striker bar. This generated a compressive loading pulse, which traveled along the bar towards the specimen. Due to the variation in mechanical impendence when the wave passed through the specimen, this incident wave, ε_i, was partly reflected (ε_r), and partly transmitted (ε_t). According to the one-dimensional theory of elastic wave propagation, the strain, stress, and strain rate, respectively, within the specimen can be determined from the following expressions [18]:

$$\varepsilon_s(t) = \frac{-2C_0}{L}\int_0^t \varepsilon_r(t)\,dt, \tag{1}$$

$$\sigma_s(t) = E\left(\frac{A}{A_s}\right)\varepsilon_t(t), \tag{2}$$

$$\dot{\varepsilon}_s(t) = \frac{-2C_0}{L}\varepsilon_r(t), \tag{3}$$

where E and C_0 are the Young's modulus and the elastic wave velocity in the bars, respectively, L is the initial length of the specimen, and A/A_s is the ratio of the bar area to the specimen area. Regarding the optical observations of the microstructure, the specimens were first etched in a solution of 32%HNO_3, 32% HCl, and 36% H_2O (by volume) for 1 min, and then examined through a Reichert Jung MeF3 optical microscope. Following specimen failure, the fracture features of specimens were examined by means of a JEOL JXA 840 SEM operating at an acceleration potential of 20 kV.

3. Results and discussion

3.1. Microstructures of undeformed weldment

Fig. 2(a) presents an optical micrograph of the base metal, heat affected zone (HAZ), and fusion zone of an undeformed 304L SS GTAW weldment. The base metal consists of ferrite phases (dark) with a volume of approximately 2%, and polygonal austenite grains (light), while the fusion zone contains δ-ferrite formations with a volume of 9%, characterized by a columnar dendritic structure. Epitaxial growth of the grains in the fusion zone from the grains of the base metal is observed along the direction of the maximum temperature gradient. Furthermore, a narrow HAZ with coarse grains is seen to form between the base metal and the fusion zone as a result of the difference in the cooling rates of these two regions during the welding process. The presence of annealing twins is also observed in the microstructure of the HAZ, which is indicative of an FCC matrix having a low stacking fault energy. Fig. 2(b) shows the microstructure of the uppermost welding pass of the fusion zone, in which the δ-ferrite is shown as columnar dendrite with a spacing of 6–10 μm. The micrograph presented in Fig. 2(c) shows the interface between the 6th and 7th welding passes at a location in the middle of the fusion zone. The general feature of the presented microstructure is that of a wide variation in the ferrite morphology within the fusion zone, which arises from the adopted multi-pass welding process. A comparison of Fig. 2(b) and (c) indicates that the microstructures in the fusion zone are extremely heterogeneous, i.e. the

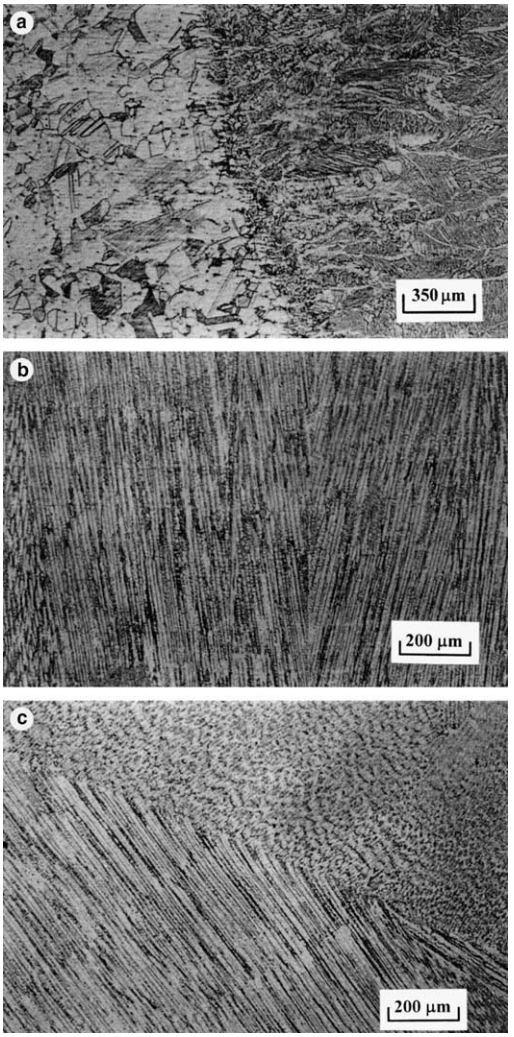

Fig. 2. Optical micrographs of 304L SS GTAW weldment at (a) interface of base metal and fusion zone; (b) top pass of fusion zone; (c) at the interface between 6th and 7th passes of fusion zone.

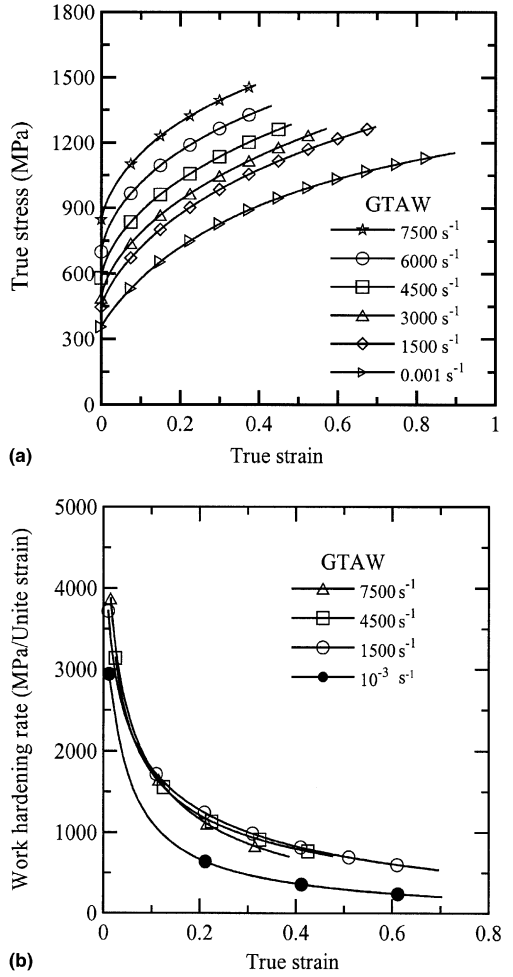

Fig. 3. (a) Typical flow stress-strain curves of 304L SS GTAW weldment deformed at different strain rates ranging from 10^{-3} s^1 to 7.5×10^3 s^{-1}; (b) variation in work hardening rate as a function of strain and strain rate.

ferrite morphology changes from a columnar dendrite arrangement in the uppermost welding pass to a vermicular formation in Fig. 2(c). This phenomenon is the result of the thermal cycle associated with each welding pass. The weld cooling rate varies from pass to pass, and accordingly, the fraction of ferrite transformation and morphology within each welding pass differs.

3.2. Stress–strain response

Fig. 3(a) presents typical true stress–true strain curves of the 304L SS GTAW weldment for different strain rates in the range of 10^{-3}–7.5×10^3 s^{-1}. At each strain rate, results from three tests are presented. Although the flow curves are all of a similar shape, it is noted that the work hardening rate of each curve is dependent upon the applied strain rate. For each curve, the weldment exhibits a work hardening effect in the initial stages of deformation. Subsequently, the flow stress attains a peak value, at which fracture of the weldment occurs. A comparison of the curves presented in Fig. 3(a) shows that the 304L SS GTAW weldment is sensitive to the strain rate, i.e. an increased flow stress is developed when deformation takes place at an increased strain rate. Moreover, in the dynamic loading regime, there is an increase in this rate sensitivity as the strain rate increases. For example, at a true strain of 0.3, the stress difference between deformations at a strain rate of 10^3 s^{-1} and those occurring at 7.5×10^3 s^{-1} is of the order of 580 MPa. It is also of interest here to examine the effect of the strain rate on the fracture strain. An

Table 3
Yielding strength (A), material constant (B), and work hardening coefficient (n) of 304L SS TGAW weldment deformed at different strain rates

Strain rate (s^{-1})	$A\sigma_y$ (MPa)	B (material constant)	n (work hardening coefficient)	ε_f (fracture strain)
0.001	355	1090	0.73	0.90
0.01	365.2	1098	0.73	0.85
0.1	369.8	1084	0.72	0.80
1500	445.7	1144	0.68	0.70
3000	487.7	1126	0.65	0.53
4500	579.3	1093	0.64	0.47
6000	699	1084	0.61	0.43
7500	846	1061	0.6	0.40

inspection of the results presented in Fig. 3(a) and Table 3 shows that the fracture strain of a 304L SS weldment which is deformed at a high strain rate is generally lower than when the weldment is strained at a quasi-static rate, i.e. the weldments fracture at true strains of 0.9 and 0.4 under strain rates of 10^3 and 7.5×10^3 s^{-1}, respectively. From these results, it can be concluded that the ability of the weldment to resist fracture is degraded as the applied strain rate increases.

The results of Fig. 3(a) indicate that the impact response of the 304L SS GTAW weldment exhibits a greater degree of work hardening under dynamic loading conditions than when the specimens is deformed quasi-statically at a strain rate of 10^{-3} s^1. The flow stress–strain relationship presented in Fig. 3(a) can be described by the general empirical work hardening law proposed by Ludwik [19], i.e.

$$\sigma = A + B\varepsilon^n, \tag{4}$$

where A is the yield strength, B is the material constant, and n is the work hardening coefficient. Application of this law to the current measurement results gives the variations in A, B and n with strain rate, as shown in Table 3. In general, it can be seen that the yield strength increases with an increasing strain rate in both the quasi-static and the dynamic regimes. However, the material constant, B, and the work hardening coefficient, n, both tend to decrease as the applied strain rate increases.

As mentioned previously, the plastic flow response of the weldment is related to the magnitude of the applied strain rate, which induces different work hardening behaviors. The slopes of the stress–strain curves in Fig. 3(a) can be used to define the work hardening rate of the weldment at a given strain rate. A typical plot of the work hardening rate against the true strain for different values of strain rate is presented in Fig. 3(b). As is to be expected, the work hardening rate is seen to decrease with an increasing strain at all values of the strain rate. It can reasonably be assumed that this is the result of microstructural changes and an increased deformation heat as the strain increases. Regarding the effect of the strain rate on the work hardening behavior, it is determined from Fig. 3(b) that for values of true strain less than 0.1, the work hardening rate increases slightly with increasing strain. Conversely, at true strain values exceeding 0.1, the work hardening rate appears to decrease as the strain rate is increased. This result can be attributed to the adiabatic deformation heat induced in the loading process.

3.3. Strain rate dependence and thermally activation volume estimation

The strain rate dependence of a material's dynamic properties is an important aspect of its constitutive relation. Although the stress–strain curves of the 304L SS GTAW weldments presented in Fig. 3(a) indicate that the strain rate sensitivity increases at higher values of the applied strain rate, the relationship between the strain rate sensitivity and the strain rate is easier to visualize if a semi-logarithmic plot of the flow stress at constant strain versus the strain rate is constructed. Accordingly, Fig. 4(a) presents the variations of the flow stress with increasing strain rate at various constant strain levels. From the results of this figure, it can be surmised that the strain rate sensitivity increases rapidly for applied strain rates of 10^3 s^{-1}, or higher. This abrupt change in the strain rate sensitivity of the flow stress is likely to be the result of the increasing influence of dislocation drag mechanisms in this region, and by the evolution of the strength/strain-rate dependence into a linear form [8]. However, some researchers have also demonstrated that the increased rate sensitivity identified in this load regime is caused by a high rate of dislocation generation, and by the rapid formation of twin structures and martensite transformation [7,9].

The strain rate dependence of the flow stress may be determined by calculating the mean apparent strain rate sensitivity parameter, which is defined as:

$$\beta = (\sigma_2 - \sigma_1)/\ln(\dot{\varepsilon}_2/\dot{\varepsilon}_1), \tag{5}$$

where σ_1 and σ_2 are the flow stresses measured at a given strain, ε, and temperature, T, at strain rates of $\dot{\varepsilon}_1$ and $\dot{\varepsilon}_2$, respectively. Under high strain rate deformation, the

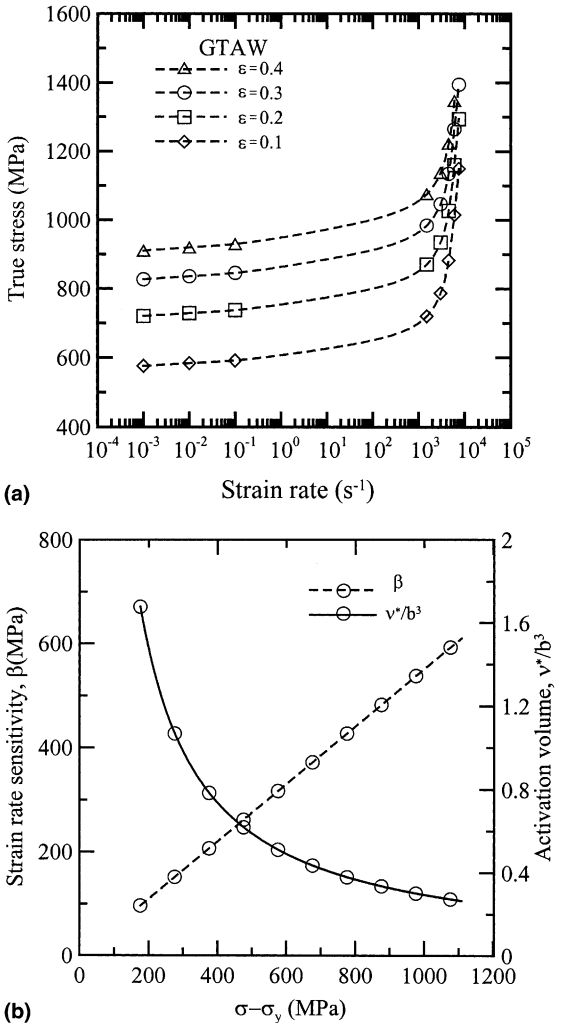

Fig. 4. (a) Influence of strain rate on flow stress under different plastic strains; (b) strain rate sensitivity and activation volume as a function of work hardening stress.

variation of the strain rate sensitivity relates to the thermal activation energy, which is a function of the local stress and the absolute temperature. The slopes of the strain rate sensitivity curves presented in Fig. 4(a) can be used to calculate the activation volume via the following expression [20]:

$$(\partial \ln \dot{\varepsilon}/\partial \sigma^*)_T = -(\partial G^*/\partial \sigma^*)/k_B T = v^*/k_B T, \quad (6)$$

where k_B is the Boltzmann constant, T is the absolute temperature, $\sigma^* = \sigma - \sigma_i$ (σ_i is the long-range internal stress caused by other dislocations or by the back stress arising from curvature of the slip dislocations), and v^* is the activation volume. In order to establish the relationship between the strain rate sensitivity, the activation volume, and the stress enhancement caused by an increase of the strain and the strain rate, the strain rate sensitivity and the activation volume of the weldment are plotted against the work hardening stress ($\sigma - \sigma_y$), as shown in Fig. 4(b). It is observed that the strain rate sensitivity is linearly proportional to the work hardening stress. This implies that the increasing strain rate sensitivity noted with increasing work hardening stress is caused by the evolution of different microstructures and by different degrees of work hardening. However, it can also be seen that the activation volume decreases rapidly as the work hardening stress increases. From this result, it may be surmised that the thermally-assisted discontinuous glide of the dislocations causes a decrease in the material's work-hardenability, and that this reduces the flow strength of the weldment. Note that in Fig. 4(b), values of v^* are normalized with respect to b^3, where b is the Burgers vector (for 304L stainless steel $b = 2.64$ Å).

3.4. Constitutive modeling

Computer simulation is often employed to predict the response of a structural design to high velocity impact loading. To ensure the reliability of the simulation results, it is first necessary to define the material's behavior under a range of strains, strain rates, and temperatures in the form of a precise constitutive model, which contains specific material constants and parameters obtained experimentally. A number of suitable constitutive models have been presented previously to describe the rate-dependent behaviors of metals [21–23]. However, the 304L SS GTAW weldment considered in the present investigation contains complex microstructures in its base metal and fusion zone regions, i.e. these microstructures include austenite (FCC), δ-ferrite (BCC), α′ martensite (BCC), and shear bands containing an ε martensite phase (HCP) and twins. Therefore, it is necessary to choose a hybrid constitutive model, such as that proposed by Zerilli and Armstrong [24], which captures these essential features of the 304L SS weldment. The Zerilli and Armstrong model can be expressed as follows:

$$\sigma = \sigma_a + Be^{\beta T} + B_0 \varepsilon^{1/2} e^{\alpha T}, \quad (7)$$

where

$$\beta = \beta_0 - \beta_1 \ln \dot{\varepsilon}, \quad (8)$$

$$\alpha = \alpha_0 - \alpha_1 \ln \dot{\varepsilon} \quad (9)$$

and

$$\sigma_a = \sigma_G + kl^{-1/2}, \quad (10)$$

where σ is the von Mises equivalent stress, ε is the von Mises equivalent strain, $\dot{\varepsilon}$ is the strain rate, T is the absolute temperature, l is the average grain diameter, and σ_G is the athermal stress caused by the effect of the solutes

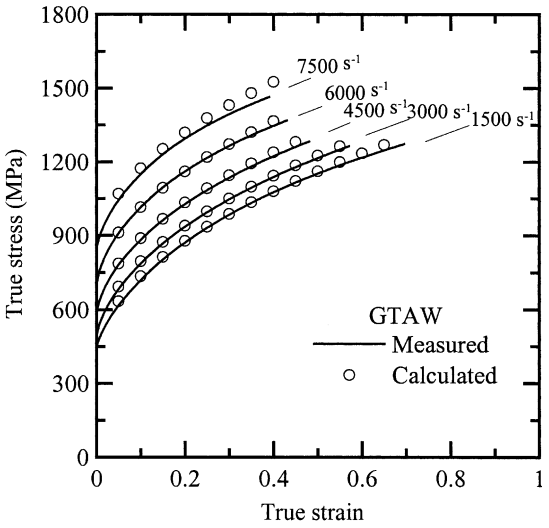

Fig. 5. Comparison between measured and predicted stress–strain curves at different strain rate ranges.

and the initial dislocation density. The variables B, β_0, β_1, B_0, α_0, α_1, k and σ_a are all considered to be constant.

Employing the parameter evaluation procedure presented in Ref. [24], and then applying the data values plotted in Fig. 3(a), it can be shown that the corresponding parameter values for the proposed constitutive equation are given by: $\sigma_a = 370$ MPa, $B = 1018$ MPa, $\beta_0 = 6.0 \times 10^{-2}$ K^{-1}, $\beta_1 = 6.42 \times 10^{-3}$ K^{-1}, $B_0 = 1120$ MPa, $\alpha_0 = 4.3 \times 10^{-4}$ K^{-14}, and $\alpha_1 = 4.67 \times 10^{-5}$ K^{-1}. Fig. 5 compares the true stress–true strain relationship predicted by the Zerilli and Armstrong model with the experimental results. It is clear that the proposed model performs reasonably well in predicting the rate-dependent behavior of the 304L GTAW weldment under a range of different strain rates.

3.5. Observations of fracture characteristics

Fractographic examination of the impacted weldments reveals that adiabatic shearing is the primary fracture mechanism. Under each of the dynamic testing conditions considered in the present investigation, the weldments failed in a catastrophic manner along planes inclined at 40–50° to the direction of impact (i.e. along the plane of maximum shear stress). Fig. 6(a) shows a low magnification side view micrograph of the weldment after fracture under an applied strain rate of 4.5×10^3

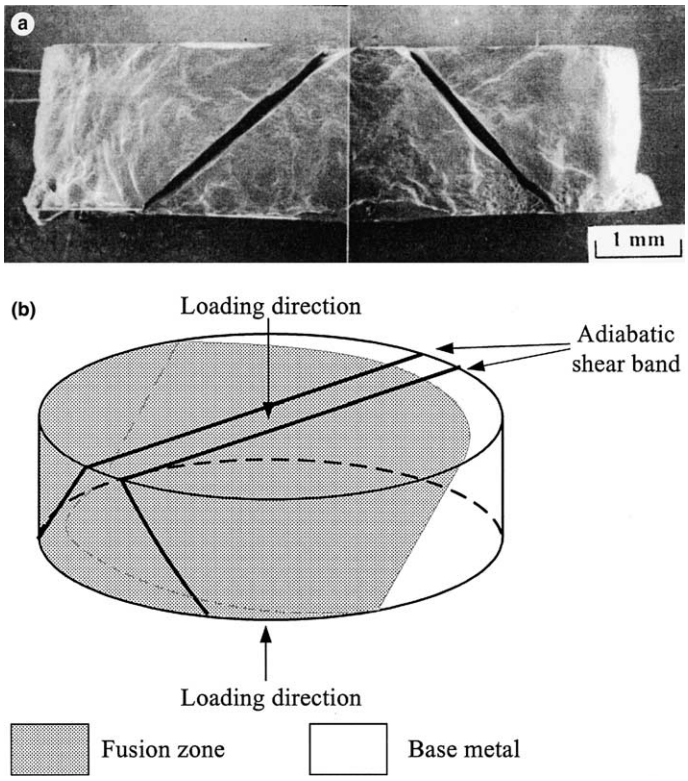

Fig. 6. (a) Fractograph of tested weldment after fracture at strain rate of 4.5×10^3 s^{-1}; (b) schematic representation of fracture features and orientation of adiabatic shear band.

s^{-1}. It can be seen that cracking along the adiabatic shear band has resulted in a separation of the specimen. Under high velocity impact loading, it is known that the plastic work associated with the deformation generates a temperature rise within the specimen and a corresponding change in the microstructure. The rate by which the temperature increases depends upon the heat produced by the deformation and upon the thermal conductivity of the material, i.e. if the rate at which heat is produced is greater than the rate at which it is conducted away from the region of deformation, the local temperature will increase, and an adiabatic shear band will be formed. Fig. 6(b) presents a schematic illustration of the observed fracture surface features, and reveals that the adiabatic shear band extends across both the fusion zone and the base metal regions. Furthermore, it is noted that fracturing does not take place at the interface of the base metal and fusion zone regions, which demonstrates that the tested weldment possesses favorable weldability characteristics, i.e. the interfacial strength in the vicinity of the fusion line is higher than that in either the fusion zone or the base metal region. Fig. 7(a) and (b) show the formation of adiabatic shear bands in the base metal and fusion zone regions, respectively, in a weldment deformed at 3.0×10^3 s^{-1}. Localized plastic flow is evident in the shear deformation zone, and the presence of well-developed cracks is noted within the shear bands. Fig. 7(c) shows the top surface of the cylindrical specimen. It can be seen that the microstructure of the region between two adiabatic bands is characterized by intensive localized strain variations and by inhomogeneous deformation. The presence of these multiple local deformation bands indicates that the weldment exhibits plasticity instability in the form of unstable plastic flow.

Although the observed fracture features of the base metal and fusion zone regions both depend strongly on the applied strain rate, a comparison of the two fracture surfaces reveals certain differences in the evolution of the fracture features. Fig. 8(a) and (b) show the fracture features of the base metal when deformed at strain rates of 1.5×10^3 and 7.5×10^3 s^{-1}, respectively. In both cases, the fracture surfaces contain dimples which exhibit pronounced elongation along the shear direction. The presence of these dimple structures indicates that the base metal has failed in a ductile manner. However, a comparison of the two figures shows that the characteristics of the two dimpled surfaces are not identical. For example, it can be seen that as the strain rate increases, the size of the elongated dimples also increases, but that the density of the dimples decreases. Furthermore, the region with a flat facet becomes more apparent at a higher strain rate. It is possible that the changes in fracture characteristics described above may cause a degradation of the weldment's fracture resistance in the base metal region. Fig. 8(c) and (d) show the fracture features

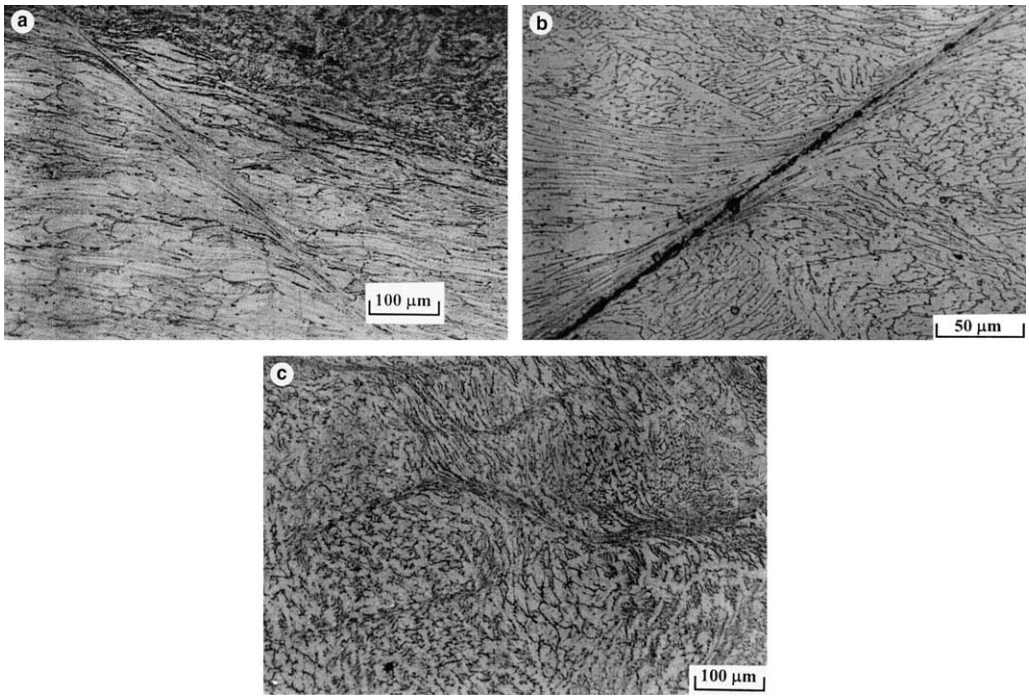

Fig. 7. (a) Formation of adiabatic shear band in base metal deformed at 3×10^3 s^1; (b) formation of adiabatic shear band in fusion zone deformed at 3×10^3 s^{-1}; (c) occurrence of intensive localized unstable flow between two adiabatic shear bands.

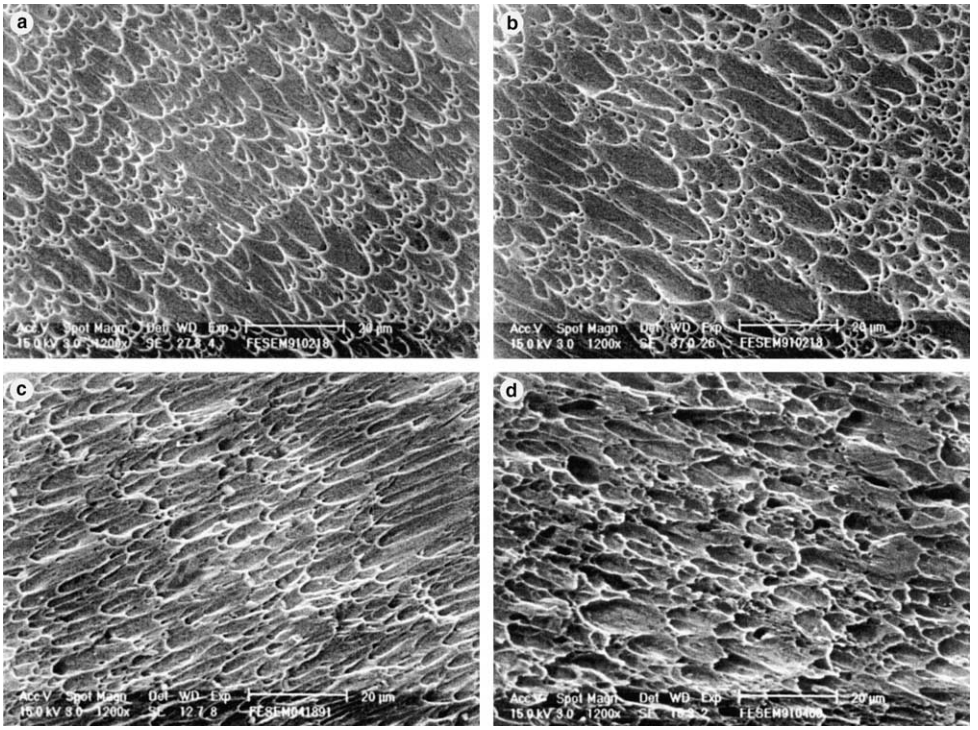

Fig. 8. Fracture feature of base metal and fusion zone deformed at two different strain rates: (a) base metal, $\dot{\varepsilon} = 1.5 \times 10^3$ s^{-1}; (b) base metal, $\dot{\varepsilon} = 7.5 \times 10^3$ s^{-1}; (c) fusion zone, $\dot{\varepsilon} = 1.5 \times 10^3$ s^{-1}; (d) fusion zone, $\dot{\varepsilon} = 7.5 \times 10^3$ s^{-1}.

of the fusion zone for weldments deformed at strain rates of 1.5×10^3 and 7.5×10^3 s^{-1}, respectively. It is clear that the forms of the fusion zone fracture surfaces are different from those of the base metal, i.e. although the surfaces still contain elongated dimples, they are flatter than those observed in the base metal. A comparison of Fig. 8(c) with Fig. 8(d) shows that the fracture features are also dependent upon the magnitude of the applied strain rate, i.e. although the surface in Fig. 8(d) is still dimpled, some cleavage features are observed in the matrix. The formation of a dimple-like fracture surface with cleavage facets implies that the ductility and fracture resistance of the fusion zone both degrade when a high strain rate loading condition is imposed. The variations in the dimpled surfaces observed in both the base metal and the fusion zone regions as the strain rate is increased correlate well with the characteristics of the flow stress–strain curves presented previously in Fig. 3, i.e. the fracture strain of the 304L TGAW weldment decreases as the strain rate is increased.

4. Conclusions

This study has presented an investigation into the plastic flow properties and failure behavior of 304L SS TGAW weldments subjected to impact compressive loading. The results have revealed that the characteristics of the tested weldment are sensitive to the applied strain rate. As the strain rate increases, it has been observed that the flow stress increases and that the fracture strain decreases. This result has been verified through a careful observation of the corresponding fracture features. It has also been shown that the work hardening rate decreases rapidly as the true strain increases for all of the strain rates considered in the present study, but that it tends to decrease with increasing strain rate when the true strain exceeds 0.1. An increased strain rate sensitivity and a decreased activation volume have been identified as the work hardening stress increases. The current study has confirmed that the observed strain rate dependent behavior of the weldment can be predicted accurately by the hybrid Zerilli–Armstrong constitutive law, i.e. it has been shown that there is good agreement between the calculated results and those obtained experimentally. SEM analysis of the fractured weldments has shown that the main fracture mechanism is one of adiabatic shearing, in which cracking takes place at an angle of 40–50° with respect to the direction of impact. The fracture surfaces of both the fusion zone and the base metal regions are characterized by a dimpled structure, where the size and density of the dimples are dependent upon the magnitude of the applied strain rate. A more brittle behavior has been identified in the fusion zone

than in the base metal, i.e. the dimple formations tend to be flatter in the fusion zone.

Acknowledgments

The authors would like to acknowledge both their department and the National Science Council of the Republic of China for their financial support. The grant from the NSC is numbered NSC 91-2216-E006-063.

References

[1] O. Kamiya, K. Kumagai, J. Mater. Sci. 25 (1990) 2017.
[2] M. Siressha, V. Shankar, Shaju K. Albert, S. Sundaresan, Mater. Sci. Eng. A 292 (2000) 74.
[3] G. Madhusudhan Reddy, T. Mohandas, K.K. Papukutty, J. Mater. Process. Technol. 74 (1998) 27.
[4] H.D. Steffens, H. kayser, Weld. J. 51 (1972) 408.
[5] D.E. Albert, G.T. Gray III, Acta Mater. 45 (1997) 343.
[6] K.P. Staudhammer, C.E. Frantz, S.S. Hecker, L.E. Murr, in: M.A. Meyers, L.E. Murr (Eds.), Shock Waves and High Strain-Rate Phenomena in Metals, Plenum press, New York, NY, 1981, p. 91.
[7] W.S. Lee, C.F. Lin, Metall. Mater. Trans. A 33A (2002) 2801.
[8] P.S. Follansbee, U.F. Kocks, Acta Metall. 36 (1988) 81.
[9] F.J. Zerill, R.W. Armstrong, Acta Metall. Mater. 40 (1992) 1803.
[10] M.A. Meyers, C.L. Wittman, Met. Trans. 21A (1990) 3153.
[11] M. Stelly, J. Le Grand, R. Dormeval, in: M.A. Meters, L.E. Murr (Eds.), Shock Waves and High Strain-Rate Phenomena in Metals, Plenum press, New York, NY, 1981, p. 113.
[12] M.R. Staker, Acta Metall. 29 (1981) 683.
[13] C. Fressengeas, A.J. Molinar, J. Mech. Phys. Solids 35 (2) (1987) 185.
[14] S.L. Semiatin, J.H. Holbrook, Metall. Trans. 14A (1983) 1681.
[15] S.S. Hecker, M.G. Stout, K.P. Staudhammer, J.L. Smith, Metall. Trans. 13A (1982) 619.
[16] L.E. Murr, K.P. Staudhammer, S.S. Hecker, Metall. Trans. 13A (1982) 627.
[17] U.S. Lindholm, J. Mech. Phys. Solids 12 (1964) 317.
[18] T. Nicholas, in: J. Zukas, et al. (Eds.), Impact Dynamics, Wiley, New York, 1982, p. 277.
[19] P. Ludwik, Elemente der Technologischen Mechanik, Springer, Berlin, 1909, p. 32.
[20] H. Conrad, J. Met. 16 (1964) 582.
[21] G.R. Johnson, W.H. Cook, in: Proceedings of 7th International Symposium on Ballistics, Am. Def. Prep. Org. (ADPA), The Mague, Netherlands, 1983, p. 541.
[22] F.J. Zerilli, R.W. Armstrong, J. Appl. Phys. 61 (1987) 1816.
[23] J.R. Klepaczko, C.Y. Chiem, J. Mech. Phys. Solids 34 (1986) 29.
[24] F.J. Zerilli, R.W. Armstrong, in: Y.D.S. Rajapakse, J.R. Vinson (Eds.), Metal and Ceramic Matrix Composite and Other Advanced Materials, ASME, New York, 1995, p. 121.